Research Square

Preprints are preliminary reports that have not undergone peer review.
They should not be considered conclusive, used to inform clinical practice,
or referenced by the media as validated information.

Free-surface flow in perforated open channels under microgravity

Zongyu Wu
National University of Defense Technology
Bo Wu
National University of Defense Technology
Yu Zhang
National University of Defense Technology
Chengguang Fan
National University of Defense Technology
Chao Jiang
National University of Defense Technology
Yuzhu Bai
National University of Defense Technology
Yong Chen
literature_chen@nudt.edu.cn

Chengdu Fluid Dynamics Innovation Center
Yong Zhao
National University of Defense Technology

Article

Keywords: microgravity, vane-type surface tension tank, free-surface flow, perforated channel, surface tension

Posted Date: November 23rd, 2026

DOI: https://doi.org/10.21203/rs.3.rs-11717885/v1

License: This work is licensed under a Creative Commons Attribution 4.0 International License.
Read Full License

Additional Declarations: No competing interests reported.

Free-surface flow in perforated open channels under microgravity

Zongyu Wu[1,2], Bo Wu[1,2], Yu Zhang[1,2], Chengguang Fan[1,2], Chao Jiang[3], Yuzhu Bai[1,2], Yong Chen[4,*], Yong Zhao[1,2,*]

[1]College of Aerospace Science and Engineering, National University of Defense Technology, Changsha, China

[2]State Key Laboratory of Space System Operation and Control, Changsha, China

[3]College of Information and Communication, National University of Defense Technology, Wuhan, China.

[4]Chengdu Fluid Dynamics Innovation Center, Chengdu, China.

*Corresponding authors: Yong Chen, E-mail: literature_chen@nudt.edu.cn

Yong Zhao, E-mail: zhaoyong@nudt.edu.cn

Abstract

With the expansion of crewed spaceflight and deep-space exploration, spacecraft propulsion systems demand ever higher reliability and efficiency from propellant management. The vanes of vane-type surface tension tanks are commonly perforated to reduce structural mass. This work studies the surface-tension-driven flow of propellant along a perforated vane in microgravity. A flow-resistance correction coefficient that depends on the perforation ratio is introduced, its correlation with the perforation ratio is calibrated by CFD, and a modified flow-resistance function is constructed. On the basis of interior-corner capillary flow theory, an analytical relation between the position of the liquid front and time is derived. Microgravity experiments in a drop tower are used to validate and recalibrate the model. After the steady height is corrected and the coefficients are recalibrated with the experimental data, the theoretical predictions agree well with the measurements. Increasing the perforation ratio markedly weakens the liquid-transport capability of the vane: once the perforation ratio exceeds 20%, the vane performs poorly, so perforated vanes should be designed with a perforation ratio below this threshold.

Keywords: microgravity; vane-type surface tension tank; free-surface flow; perforated channel; surface tension

Introduction

As human space activities expand, missions such as crewed spaceflight, deep-space exploration and on-orbit servicing place increasingly demanding requirements on propellant management technology (PMT). In a microgravity environment ($10^{-3}\,\mathrm{g} \sim 10^{-6}\,\mathrm{g}$), gravitational effects are negligible and surface tension replaces gravity as the dominant force controlling liquid motion. The distribution, migration and refilling of propellant in a tank therefore behave very differently from the ground case and must be controlled by a dedicated propellant management device (PMD).

The vane-type surface tension tank is a typical solution for propellant management in microgravity. Through functional components such as vanes, it controls the liquid free surface by the combined action of surface tension and the gas–liquid pressure difference: inside the tank, propellant is transported directionally along open flow channels formed by adjoining vanes. Compared with other PMD configurations, vane-type tanks are structurally simple, have no moving parts and are highly reliable, and are therefore widely used in operational and developing spacecraft. The design theory of the vane is the core technical foundation of such tanks. Jaekle[1] first established a flow model and a simple retention-capacity model for vanes, which enabled the first quantitative analysis of vane-type tanks and laid the foundation for later design; his approach is still instructive today. Weislogel et al.[2] further introduced the theory of surface-tension-driven free-surface flow into vane-type tank design, built a more accurate model of the transport capability and carried out tank optimization aimed at maximizing that capability.

To meet the lightweight requirements of spacecraft, vanes are now commonly perforated with regular holes to reduce structural mass, and perforated vanes have become the mainstream design. In 1999, Collicott[3] of Purdue University carried out microgravity flight tests of

perforated-vane tanks on board a KC-135 aircraft. By comparing the liquid-control capability of vanes with perforation ratios of 20% and 50%, he verified the feasibility of perforation: the tank with 20% perforation performed well and met the operational requirements, whereas the tank with 50% perforation performed poorly. This comparison suggested a new route for tank optimization. The fuel tank of the US Orbital Express mission launched in 2007 adopted a perforated-vane configuration, and the PMD designed by Liu et al.[4] used perforated vanes, whose reliability was demonstrated by ground sloshing tests. The vanes of the on-orbit refuelling payload[5] of the Tianyuan-1 satellite launched in 2016 were also perforated. In 2024, Chen et al.[6] and Chen et al.[7] of the Institute of Mechanics, Chinese Academy of Sciences, performed two-way liquid transport experiments in a vane-type tank aboard the Chinese Space Station, studying bubble motion and liquid climbing during filling; the vanes in that tank were also perforated.

Perforation, however, directly alters the boundary conditions and the pressure-loss characteristics of the free-surface flow in the channel, which brings new challenges to tank design. Although perforated vanes have become a common design option, the quantitative influence of perforation on the transport capability still lacks systematic theoretical support: perforation breaks the continuity of the original channel and changes the capillary pressure distribution at the gas–liquid interface — for example, the meniscus at a hole edge is distorted in curvature and produces an additional pressure loss. This effect has not yet been taken into account as a design index in engineering practice, yet the influence of perforation on the transport capability of a vane is real, so the underlying mechanism needs to be studied.

From a theoretical point of view, understanding the dynamics of liquid flow in open capillary channels is of considerable theoretical and practical significance for improving space liquid management[8]. During propellant reorientation, the flow of propellant along the interior corners formed by the internal structures of the tank under surface tension is one of the most

critical liquid behaviours in a vane-type tank[9]. Such surface-tension-driven flows result from the combined action of surface tension, channel geometry and liquid viscosity[10,11].

In the 1960s, Concus and Finn[12] proposed the Concus–Finn condition, which gives the critical condition for the existence of a stable state of liquid flow in an open wedge-shaped channel and laid the theoretical foundation of interior-corner capillary flow. Since then, the solution of the governing equations and the refinement of the models have been pursued over a long period. Ayyaswamy et al.[13] derived and solved the two-dimensional momentum equation of interior-corner flow and showed that the channel half-angle and the solid–liquid contact angle are the two independent key parameters controlling the flow. Lenormand and Zarcone[14] focused on the nonlinear diffusion problem of interior-corner flow and gave an approximate solution of the equation. Dong and Chatzis[15] introduced a dimensionless flow-resistance coefficient into the theory of Lenormand et al. to correct the model and improved the accuracy, but their correction applies only to interior-corner flow with a half-angle of 45°, which limits its range of use. Romero and Yost[16] treated the nonlinear diffusion equation of the liquid phase by a similarity transformation and, under specific boundary conditions, solved the resulting ordinary differential equation numerically.

Weislogel simplified the Navier–Stokes equations with lubrication theory, solved the governing equations by a similarity transformation and, in 2019, proposed a new lubrication model that resolved the drainage of a wetting liquid from an interior corner[17]. Chen et al.[11] and Kang et al.[18] studied capillary flow along rounded corners both theoretically and experimentally; Ramé et al.[19] studied interior-corner flow under microgravity; and Li[20] and Li[21] designed experiments on capillary flow in asymmetric interior corners.

Building on studies of straight channels, Wu[22,23] examined the effect of channel curvature on surface-tension-driven flow and showed that a larger curvature accelerates the flow; Chen et al.[24,25] extended the problem to capillary-driven flow between plates with a finite included

angle and established a theoretical model of the surface shape at an annular interior corner in microgravity; Fiorini et al.[26] studied the flow of a low-viscosity liquid along a tube wall and corrected the dynamic contact angle of that flow; Chen et al.[27] proposed a theoretical model of the steady surface in an axisymmetric container under microgravity, enabling efficient and accurate prediction of the steady surface; and Wu et al.[28] studied free-surface bubbly flow in a rectangular channel and analysed the effect of void fraction on the critical flow rate. As for experimental methods, Lin et al.[29] used magnetic compensation to simulate microgravity on the ground and studied microgravity free-surface flow.

In summary, although vane-type surface tension tanks have made considerable progress in both theory and engineering, the existing theory is still incomplete. Current interior-corner free-surface flow theory rests on the assumption of a continuous, smooth channel and cannot describe the flow between perforated vanes; moreover, the quantitative description of the complex unsteady flow in a perforated channel is still missing, and the quantitative influence of perforation on the transport capability lacks systematic theoretical support.

To address these gaps, this work studies surface-tension-driven free-surface flow in a perforated channel in microgravity, with propellant reorientation as the background. A one-dimensional theoretical model is established in which the effect of perforation on the flow-resistance function is taken into account. Three-dimensional numerical simulations of the flow of liquid along a perforated vane in a tank are performed with CFD software to obtain the flow-resistance correction coefficient. The model is then validated experimentally, and the origin of the deviation between theory and experiment is identified. Finally, the effects of the perforation ratio, the channel half-angle, the liquid viscosity and the vane width on the transport capability are analysed systematically.

Results and discussion

Results of flow resistance function modelling

The flow of propellant along a perforated vane in a tank can be idealised as free-surface flow in a perforated channel, as shown in Fig. 1. The flow of liquid in such a channel is analysed here on the basis of the one-dimensional theoretical model of capillary flow in a straight interior corner.

Figure 1 shows a perforated wedge-shaped channel with an interior angle of 2α. The channel is abstracted from the interior-corner flow between perforated vanes in a tank. Liquid enters from one end of the corner and advances along the channel driven by surface tension; the dark region in the figure represents the liquid. The contact angle between the liquid and the solid surface is θ, and the situation satisfies the Concus–Finn condition, i.e. θ satisfies $\theta \le (\pi/2 - \alpha)$, which allows the liquid to extend indefinitely along the channel in theory[12].

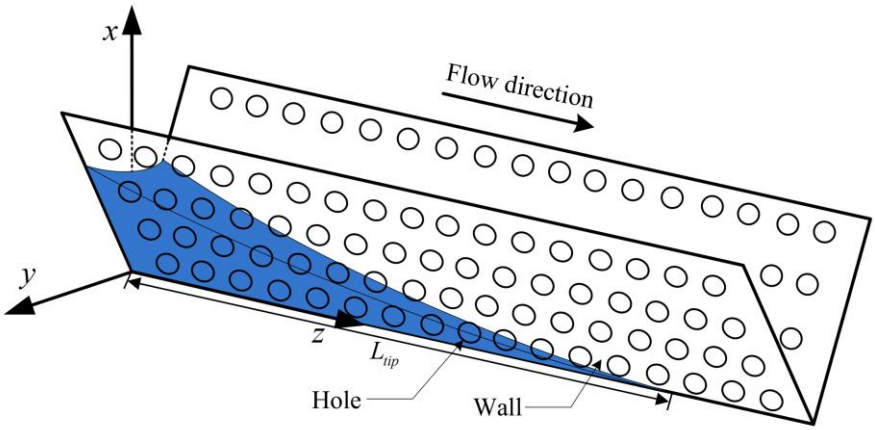


Fig. 1 | Interior-corner capillary flow in a perforated channel under microgravity

To determine the equivalent flow-resistance correction function $\lambda(\varphi)$ of the perforated channel, three-dimensional numerical simulations of free-surface flow in a perforated channel were carried out with the open-source software OpenFOAM, and the function was evaluated from the simulation data.

Six cases were simulated; the geometric model and its parameters are described in Methods. The rise of the free surface in each case is shown in Fig. 2. The wedge-shaped perforated channel is on the left and the tank wall on the right; in microgravity the surface rises on both sides, but it rises faster in the wedge-shaped channel formed by the perforated vanes and is clearly higher than on the right, which shows that the vanes guide the liquid effectively. Figure 2a shows the free surface without perforation, which is higher at the same instant than in the other cases. As time proceeds, the distance climbed in a fixed time interval decreases and the climbing speed slows down, finally tending to a steady flow velocity.

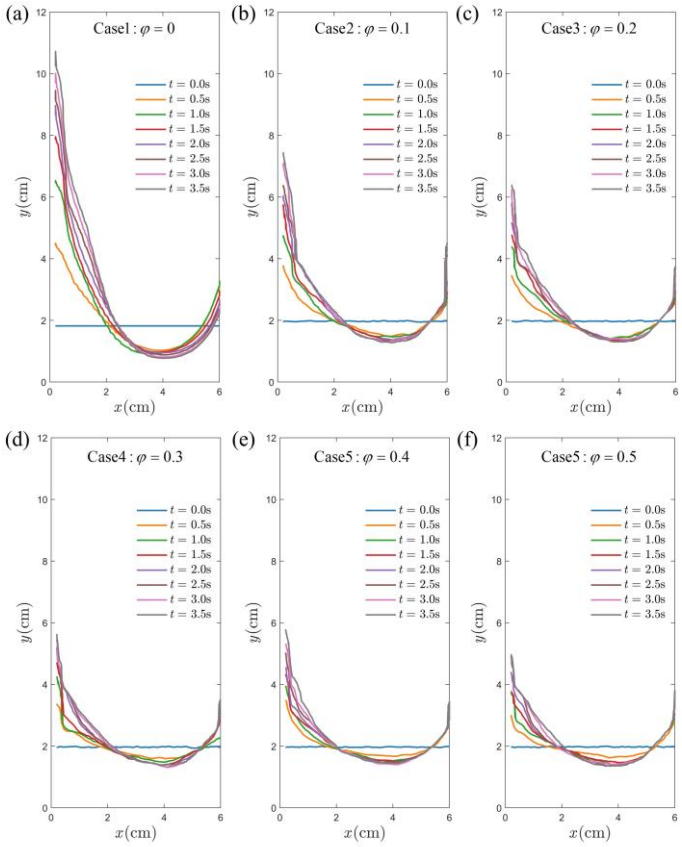


Fig. 2 | Free-surface evolution in channels of different perforation ratios in the simulations ($z = 0$)

As the perforation ratio increases, the climbing distance of the free surface decreases substantially, which shows that wall perforation strongly affects the capillary flow. When the perforation ratio reaches 0.5, the transport capability of the channel approaches that of the tank

wall on the right, indicating that the vane has almost lost its function.

Moreover, in every case the surfaces at different instants intersect almost at the same two points: the right-hand point is the steady height at the tank wall, and the left-hand point $x \approx 2.2\text{cm}$ is the steady height in the wedge-shaped channel. The steady height is the same for all perforation ratios, which shows that it depends only on the channel geometry and not on the perforation ratio. The reason is that the steady height corresponds to the position of pressure equilibrium between the liquid column and the liquid at the bottom of the tank. The pressure balance involves only the surface curvature and the cross-sectional geometry of the channel, and the holes affect only the resistance during the flow, not the equilibrium state itself.

From the recorded rise of the front, the function $\lambda(\varphi)$ can be calculated. Fitting the simulation results for different perforation ratios gives an approximate expression for λ (Fig. 3),

$$\lambda(\varphi) = \frac{1}{c_1 e^{c_2 \varphi} + c_3 e^{c_4 \varphi}} \tag{1}$$

where the coefficients take the values

$$\begin{cases} c_1 = 0.6796 \\ c_2 = -19.8381 \\ c_3 = 0.3205 \\ c_4 = -1.8412 \end{cases} \tag{2}$$

The fitting expression satisfies $\lambda(0) \approx 1$, that is, it reduces to the straight-channel case when there is no perforation, in agreement with physical expectation. Eqs. (1) and (2) together constitute the flow-resistance correction model that accounts for the perforation ratio.

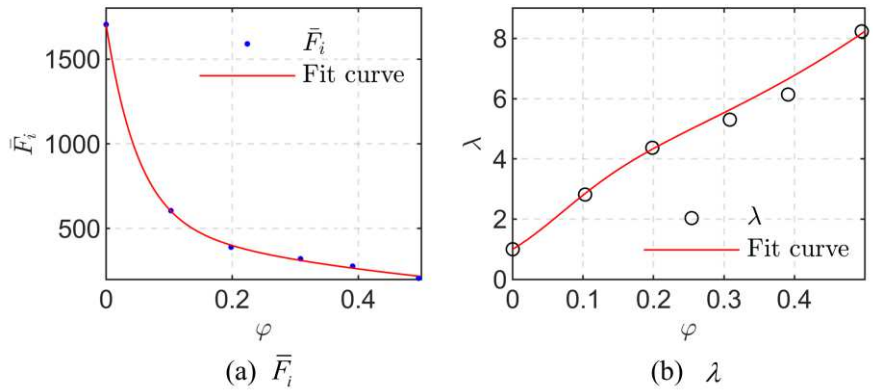


Fig. 3 | Fitted results of the flow-resistance function and the correction coefficient. (a) Flow-resistance function; (b) correction coefficient.

Drop-tower experiments

To validate the theoretical model of the perforated channel, a microgravity experiment was designed with test articles geometrically identical to the simulation model. Because the number of drops was limited, three experiments were carried out, corresponding to Cases 2, 3 and 5 in Table 1, that is, perforation ratios of 0.1, 0.2 and 0.4. Further details of the drop-tower experiments are given in Methods.

Figure 4 shows part of the experimental record. The climbing of the surface in the three experiments is shown. It can be seen that a larger perforation ratio slows the climb, and that the height reached at a given instant decreases. Image recognition was used to extract the surface position at each instant and hence the flow distance as a function of time, as shown in Fig. 5. The trend of the theoretical results is close to that of the experiments, but the measured values are larger than the theoretical ones.

First, the theoretical results are systematically lower than the measured ones, mainly because the calculated steady height is much lower than the experimental value. The steady height calculated from Eq. (15) is $H_T = 1.54\text{cm}$, whereas the simulated value is 2.2 cm (close to the experiment). The main reason is that the calculation neglects the climb of the surface on the outer wall and assumes that the surface rises only in the channel; in reality the climb on the

outer wall directly affects the surface in the channel and shifts the steady-height point.

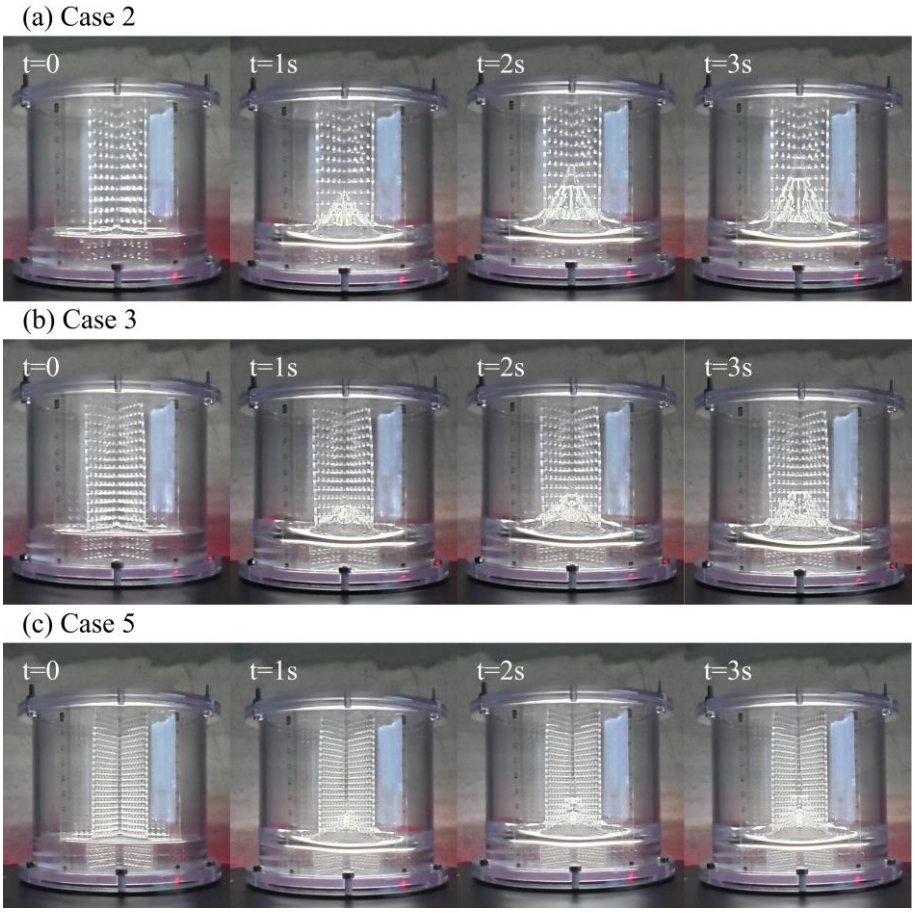


Fig. 4 | Evolution of the free surface in the experiments. (a) Case 2; (b) Case 3; (c) Case 5.

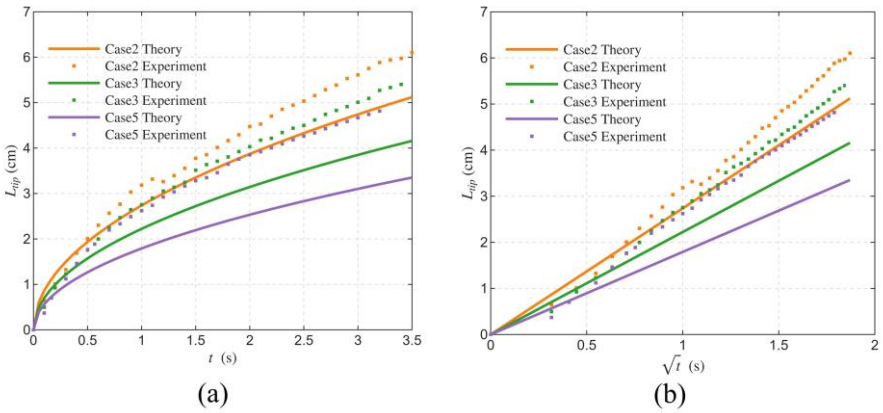


Fig. 5 | Measured surface height versus time in the experiments. (a) Surface height as a function of time; (b) Surface height as a function of the square root of time.

In addition, the spacing between the three experimental curves is smaller than that of the theoretical results. Since the theoretical results are computed from the simulation data, it can be inferred that the boundary condition imposed at the perforations in the three-dimensional

simulation exaggerates the actual influence of perforation.

A comparison of the simulated and the experimental images shows that, in the simulation, when the surface reaches a circular hole in the wall it either wets the hole completely or not at all, so that the originally smooth boundary of the surface is disrupted by the hole. This strengthens the influence of the holes on the transport capability. In the experiment, by contrast, the surface clearly remains fairly smooth, without visible distortion of its boundary. This is probably an important source of the discrepancy.

Accordingly, the steady height was corrected and the coefficients of $\lambda(\varphi)$ were recalibrated from the experimental data, which gives

$$\begin{cases} c_1 = 0.6553 \\ c_2 = -22.1442 \\ c_3 = 0.3447 \\ c_4 = -0.5471 \end{cases} \tag{3}$$

The final theoretical results are shown in Fig. 6, where the theoretical and experimental data agree well.

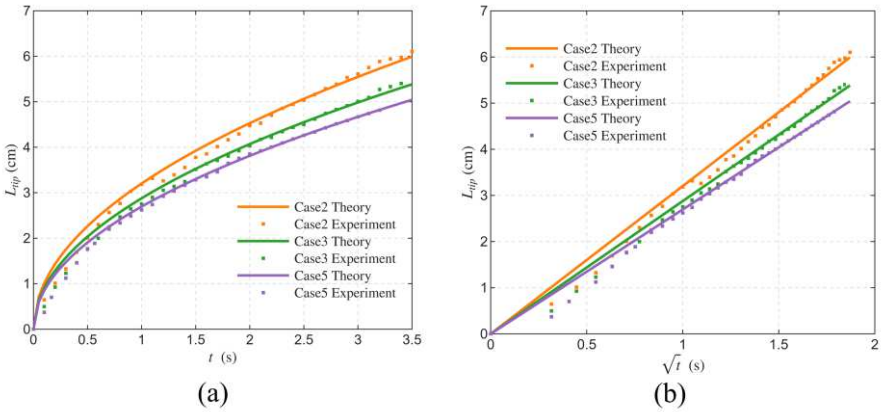


Fig. 6 | Theoretical results after correction. (a) Surface height as a function of time; (b) Surface height as a function of the square root of time.

Effect of the perforation ratio

Figure 7 shows the results calculated with the theoretical model. The perforation ratio

strongly affects the climbing velocity of the liquid column: the larger the perforation ratio, the slower the climb. As the perforation ratio increases, the guiding effect of the wedge-shaped channel gradually weakens, so that the liquid column can hardly continue to climb along the vane. Figure 2 also shows that, once the perforation ratio reaches 0.5, the transport capability of the vane is comparable to that of the tank wall, indicating that the vane has almost lost its guiding function.

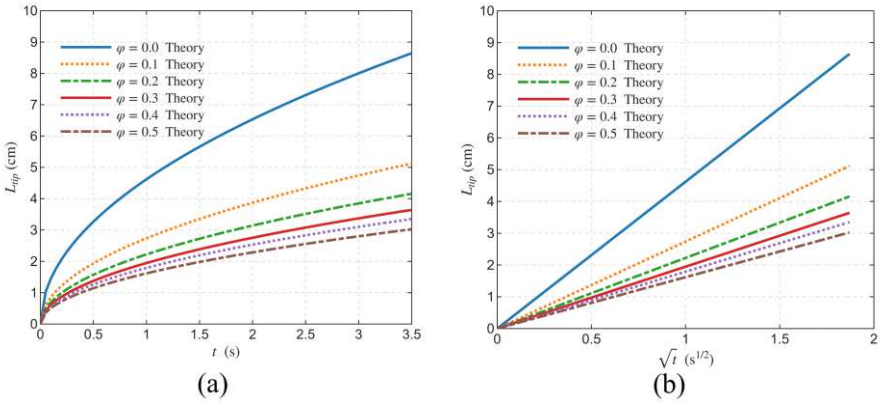


Fig. 7 | Comparison of the liquid-front position versus time. (a) Surface height as a function of time; (b) Surface height as a function of the square root of time.

The physical origin of this $L \propto t^{1/2}$ behaviour lies in the asymmetric evolution of the driving force and the resistance: the capillary driving force, which is set by the surface curvature corresponding to the steady height, is approximately constant during the climb, whereas the viscous resistance increases linearly with the length of the liquid column. Equilibrium between the two gives $w = \mathrm{d}L/\mathrm{d}t \propto L^{-1}$. Perforation acts precisely by increasing the equivalent flow resistance, that is, by lowering $\overline{F}_i$, and thereby slows this diffusion process without changing its power-law form, which explains why the experimental curves for different perforation ratios have a similar shape but different slopes.

Figure 8 shows the front position after 3.5 s as a function of the perforation ratio. Below 0.2, the flow-resistance function decreases sharply as the perforation ratio increases, which means that the flow resistance grows rapidly and directly limits the climbing efficiency of the

liquid column; above 0.2, the decrease of the climbing distance slows down markedly. At this point the guiding action of the vane is already similar to that of an ordinary wall, which departs completely from the original purpose of enhancing propellant transport through a guiding structure.

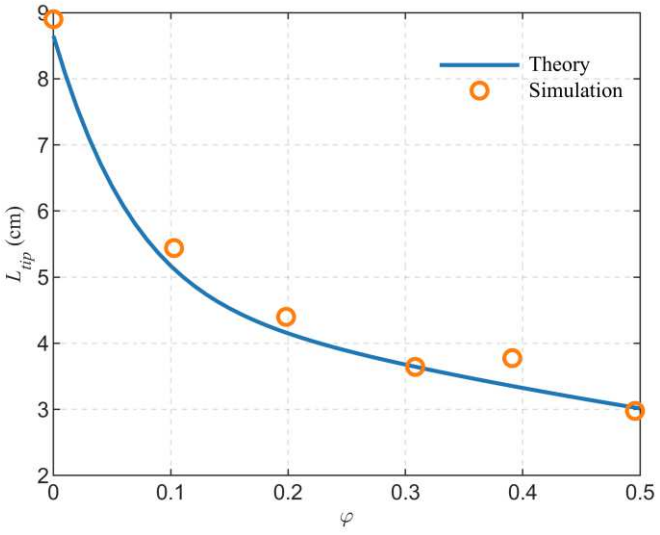


Fig. 8 | Front position versus perforation ratio at 3.5 s

The mechanism by which perforation weakens the transport capability can be reduced to two points. First, the curvature of the meniscus at the hole edges is distorted, so that the gas–liquid interface produces a local additional capillary pressure drop when it crosses a hole edge, which is equivalent to an extra pressure-loss term in series along the flow path. Second, perforation destroys the geometric continuity of the channel, increases the equivalent hydraulic diameter and weakens the capillary confinement of the liquid by the corner. In terms of the correction coefficient, the former appears as a rapid increase of $\lambda(\varphi)$ with φ, that is, the exponential term c_2 in Eq. (1) dominates; the latter appears as the limiting behaviour in which the channel degenerates into an approximately flat wall at a high perforation ratio. The perforation ratio of a vane should therefore be kept below 0.2 in design. The quantitative threshold obtained here is consistent with the qualitative conclusion of the flight tests of

Collicott[3], in which a perforation ratio of 20% performed well while 50% performed poorly, and refines that conclusion into a quantitative criterion that can be used directly in design.

Effects of other parameters

The tank model used in this work has six internal vanes, that is, a half-angle of 30° for a single channel. Figure 9 shows that this half-angle is not the optimum value: the theoretical optimum half-angle is about 15°, which corresponds to 12 internal vanes. The influence of the half-angle on the climbing performance results from the competition between the capillary driving force and the viscous resistance: the smaller the half-angle, the sharper the corner and the smaller the radius of curvature of the surface, so the capillary driving force is stronger, but at the same time the channel cross-section is narrower and the viscous resistance larger. The two effects together produce an optimum half-angle, and any deviation from it reduces the transport efficiency.

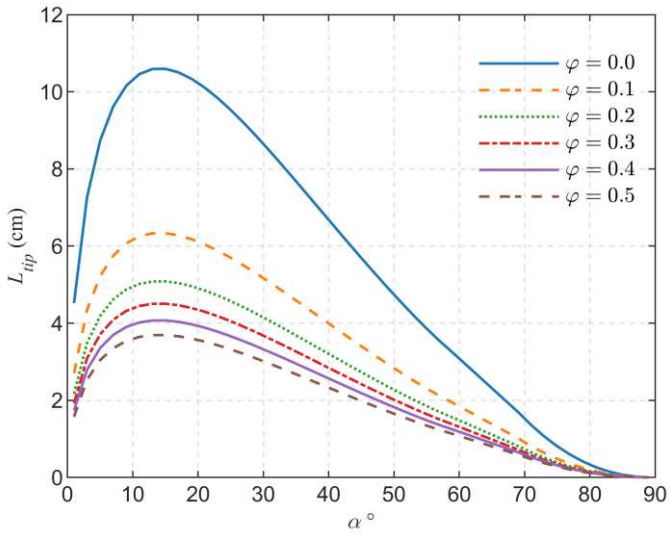


Fig. 9 | Front position versus channel half-angle

The influence of the viscosity is similar to that of the perforation ratio, as shown in Fig. 10. When the viscosity is below 0.01 Pa·s the liquid is thin, the resistance to the liquid column is small and the climb is fast; when the viscosity is above 0.03 Pa·s the liquid is viscous and

surface tension is insufficient to drive rapid climbing. The reason is that the viscous resistance is proportional to μ, whereas the capillary driving force is independent of the viscosity; Eq. (10) also shows the flow coefficient $G \propto \mu^{-1}$. The viscosity of conventional chemical propellants is mostly below this upper limit, so surface-tension tank concepts are well adapted to them.

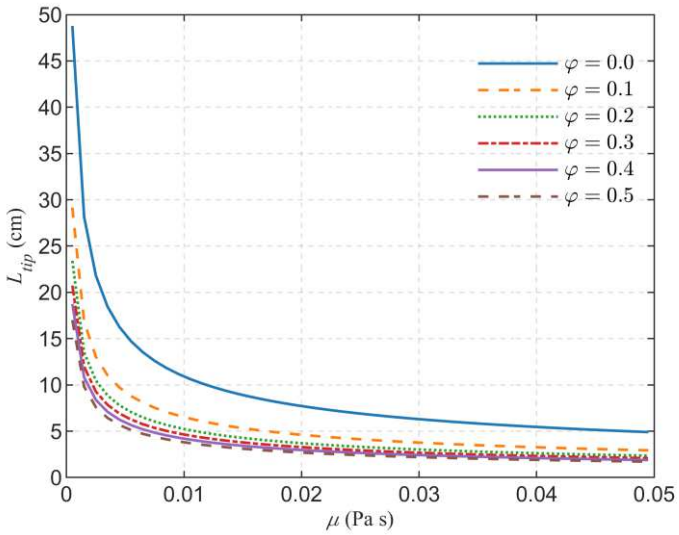


Fig. 10 | Front position versus liquid viscosity

The influence of the vane width on the front position is shown in Fig. 11. The narrower the vane, the faster the liquid column climbs. This does not mean, however, that the vane should be as narrow as possible: although reducing the vane width increases the climbing speed, it also reduces the transported flow rate and is unfavourable for guiding the liquid. This contradiction arises because the climbing speed is governed by the resistance per unit cross-section, whereas the transported flow rate is governed by the cross-sectional area, so the two place opposite requirements on the vane width. The vane width should therefore be chosen by weighing the climbing rate against the transported flow rate, according to the required filling or draining time and the required transported volume.

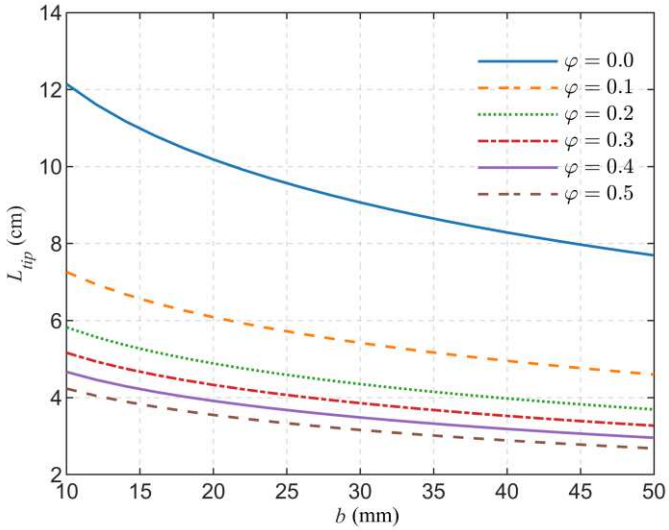


Fig. 11 | Front position versus vane width

Summary of the discussion

This work has studied surface-tension-driven free-surface flow in a perforated channel in microgravity by combining theoretical modelling, numerical simulation and drop-tower experiments. Based on the interior-corner flow theory of Weislogel, a pressure-loss correction coefficient was introduced to construct a modified flow-resistance function that accounts for perforation, and its semi-analytical solution shows that the position of the front is proportional to the square root of time; the model was calibrated by three-dimensional simulation and validated by 3.5 s drop-tower experiments, and the theoretical predictions agree well with the measured data. Perforation is found to weaken significantly the directional transport capability of the vane; if the perforation ratio exceeds 20%, the vane loses its design purpose. The steady height of the channel depends only on the channel geometry and is independent of the perforation ratio.

Methods

Theoretical analysis

For the perforated channel shown in Fig. 1, surface tension is the dominant factor

controlling the liquid motion in the absence of gravity. Figure 12 shows the cross-section of the channel perpendicular to the flow direction, in which the liquid and the gas form a concave meniscus $S'(y',z',t')$ in the contact region. The height of this meniscus is denoted by h'.

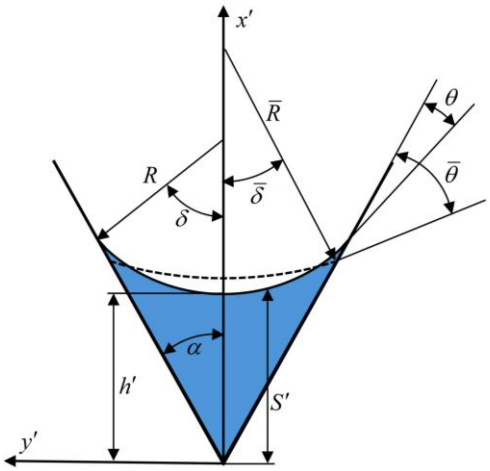


Fig. 12 | Cross-section of the interior-corner channel perpendicular to the flow direction

Following Weislogel[10], the governing equation is

$$2\frac{\partial h}{\partial t} = F_i\left(2\left(\frac{\partial h}{\partial z}\right)^2 + h\frac{\partial^2 h}{\partial z^2}\right) \tag{4}$$

where F_i is the flow-resistance function.

Applying a similarity transformation to this equation yields the position of the liquid front,

$$L_{tip} = 1.702\sqrt{F_i t} \tag{5}$$

the velocity of the liquid front,

$$w_{L_{tip}} = 0.851\sqrt{\frac{F_i}{t}} \tag{6}$$

the liquid velocity at the initial cross-section $z = 0$,

$$w_{z=0} = 0.349\sqrt{\frac{F_i}{t}} \tag{7}$$

and the volumetric flow rate at the initial cross-section $z = 0$ is

$$Q_{z=0} = A_{z=0} w_{z=0} = \frac{0.349 F_A H^2}{\tan\alpha} \sqrt{\frac{F_i}{t}} \tag{8}$$

where $A_{z=0}$ is the initial cross-sectional area, F_A is a dimensionless cross-sectional area coefficient related to the interior-corner geometry, H is the steady height and α is the corner half-angle.

Eq. (5) shows that the position of the front is proportional to the square root of time, which is an inevitable consequence of a constant capillary driving force opposed by a viscous resistance that grows as the liquid column lengthens.

Restoring the front position, the front velocity and related quantities to dimensional form gives

$$\begin{cases} L'_{tip} = 1.702\sqrt{GHt'} \\ w'_{L_{tip}} = 0.851\sqrt{\dfrac{GH}{t'}} \\ w'_{z=0} = 0.349\sqrt{\dfrac{GH}{t'}} \\ Q'_{z=0} = A'_{z=0} w'_{z=0} = 0.349 F_A \sqrt{\dfrac{GH^5}{t'}} \end{cases} \tag{9}$$

where G is the flow coefficient,

$$G = \frac{\sigma F_i \sin^2\alpha}{\mu f} \tag{10}$$

in which σ is the surface tension coefficient, μ is the dynamic viscosity and f is a dimensionless damping factor determined by the interior-corner geometry and the contact angle.

For the steady height H, consider the tank whose cross-section is shown in Fig. 13 and take one interior corner as the object of study. According to the method of de Lazzer[30], the radius of curvature of the liquid surface depends on the shape and size of the container and on

the contact angle of the liquid.

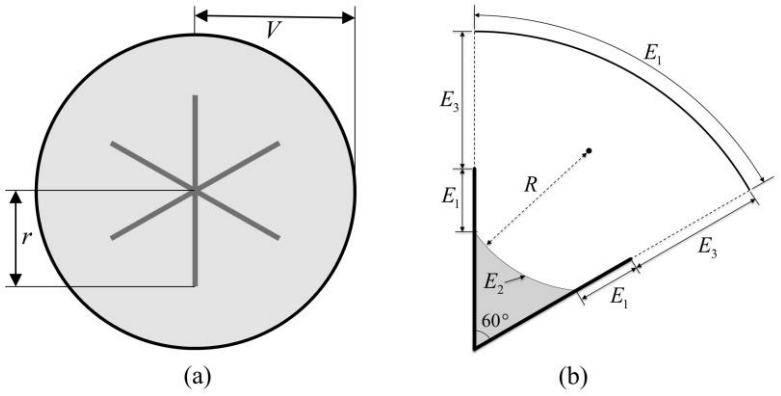


Fig. 13 | Schematic of the tank dimensions. (a) Cross-section of the tank; (b) a single interior corner.

The mean radius of curvature R is determined by

$$E_1 \cos\theta_1 + E_2 \cos\theta_2 + E_3 \cos\theta_3 = \frac{\Omega}{R} \tag{11}$$

where E_1 is the unwetted side, θ_1 being the contact angle θ of the liquid on the wall; $E_2 = 2\delta R$ is the liquid surface, θ_2 being 0; $E_3 = 2(r - V)$ is the line of symmetry, θ_3 being $\pi / 2$; and Ω is the area enclosed by the liquid surface and the various boundaries, that is, the area that contains no liquid.

The length of the unwetted side E_1 is given by

$$E_1 = 2\left(V - \frac{R\sin\delta}{\sin\alpha}\right) + 2\alpha r \tag{12}$$

where V is the vane width and r is the tank radius.

The area containing no liquid, Ω, is expressed as

$$\Omega = \alpha r^2 - \left(\left(R\cos\delta + \frac{R\sin\delta}{\sin\alpha}\cos\alpha\right)R\sin\delta - \delta R^2\right) \tag{13}$$

where $\alpha = \pi/n$ and $\delta = \pi/2 - \theta - \alpha$.

353 Combining these equations gives

354 $$R = \frac{(V + \alpha r)\cos\theta}{F_A}\left(1 - \left(1 - \frac{\alpha r^2 F_A}{(V + \alpha r)^2 \cos^2\theta}\right)^{0.5}\right) \tag{14}$$

355 where V is the vane width, r is the tank radius and R is the radius of curvature of the free
356 surface.

357 The steady height is then calculated as

358 $$H = \frac{R}{f} \tag{15}$$

359 Integrating Eq. (8) over time t' gives the total volume of liquid entering the interior-
360 corner channel,

361 $$V' = \int_0^{t'} Q'_{z=0}\mathrm{d}t' = 0.698 F_A \sqrt{GH^5 t'} \tag{16}$$

362 The mean cross-sectional area of the liquid column is then obtained as

363 $$\overline{A}' = \frac{V'}{L'_{tip}} = 0.4101 F_A H^2 \tag{17}$$

364 and the mean velocity of the liquid column is

365 $$\overline{w}' = \frac{Q'_{z=0}}{\overline{A}'} = 0.851\sqrt{\frac{GH}{t'}} \tag{18}$$

366 Since $\overline{w}' = w'_{L_{tip}}$, the final expression for the front position is obtained as

367 $$L'_{tip} = 1.702\sqrt{GHt'} \tag{19}$$

368 and the volumetric flow rate is

369 $$Q'_{z=0} = 0.349 F_A \sqrt{\frac{GH^5}{t'}} \tag{20}$$

370 The relations above constitute a complete one-dimensional theoretical solution of

capillary flow in a straight interior-corner channel and provide the framework for the perforation correction introduced below.

F_i is the flow-resistance function proposed by Weislogel, defined as

$$F_i = -\frac{\bar{w}}{\partial h/\partial z} \tag{21}$$

In a straight interior-corner channel the flow-resistance function F_i is a weak function of the corner half-angle α and the contact angle θ. It is related to the conventional flow damping coefficients β and K by

$$\begin{cases} F_i = \dfrac{f^2}{\beta \sin^2 \alpha} \\ F_i = \dfrac{8}{K}\left(\dfrac{F_A}{f \sin \delta}\right)^2 \end{cases} \tag{22}$$

where δ is a characteristic angle describing the geometry of the free surface.

Unlike other flow damping coefficients, F_i is inversely proportional to the flow damping: the larger F_i is, the smaller the damping, and the smaller F_i is, the larger the damping. For any half-angle α and contact angle θ, the value of Fi for an ordinary straight channel lies in the range $[1/8, 1/6]$.

Unlike the flow-resistance function F_i of an ordinary straight interior-corner channel, the value of F_i in a perforated interior-corner channel depends not only on the half-angle α and the contact angle θ but also on the perforation ratio φ. The influence of the perforation ratio on F_i is twofold: first, the curvature of the meniscus at the hole edges is distorted, which changes the boundary condition of the free surface and produces an additional capillary pressure loss; second, perforation changes the hydraulic diameter of the channel and weakens

its continuity.

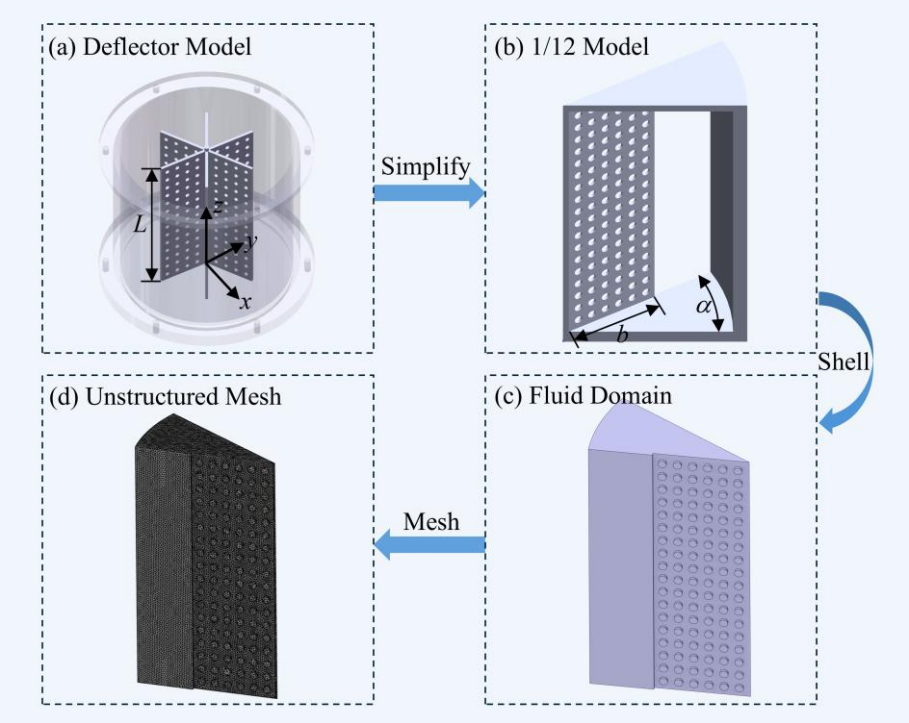
In this work the influence of the perforation ratio on the free surface is introduced into the solution of F_i: a pressure-loss correction coefficient is used to modify the flow-resistance function of the straight channel, which gives the equivalent flow-resistance function of the perforated channel.

$$\bar{F}_i = \frac{F_i}{\lambda(\varphi)} \tag{23}$$

where λ is the pressure-loss correction coefficient. $\lambda(\varphi) \geq 1$, and it increases with the perforation ratio; physically it represents the extent to which the additional pressure loss caused by perforation reduces the transport capability. Its value cannot be obtained analytically and must be calibrated by numerical simulation and microgravity experiments.

Numerical method

To make the channel closer to the actual passages of a tank, the model shown in Fig. 14a was adopted. In this model six channels are arranged symmetrically about the axis, each with a half-angle of 30°, and the channel walls are perforated plates. Six simulation models with different perforation ratios were built, and their parameters are listed in Table 1. The liquid initially rests at the bottom of the container and, in microgravity, climbs along the central wedge-shaped channel. The initial liquid height was set to 20 mm and the rise of the surface was recorded for 3.5 s, which gives the length of the liquid column as a function of time. The working liquid was Shin-Etsu KF-96-10cst silicone oil; its properties and the channel dimensions are listed in Table 2.



410

411 **Fig. 14** | Geometric model and mesh

412 **Table 1** | Geometric parameters of the perforated vanes

Case	Hole diameter	Number of holes	Vane size	Perforation ratio	Channel angle 2α
Case 1	3 mm	0	35 × 110 mm²	0	60°
Case 2	3 mm	56	35 × 110 mm²	0.1028	60°
Case 3	3 mm	108	35 × 110 mm²	0.1983	60°
Case 4	3 mm	168	35 × 110 mm²	0.3084	60°
Case 5	3 mm	216	35 × 110 mm²	0.3966	60°
Case 6	3 mm	270	35 × 110 mm²	0.4957	60°

413

414 **Table 2** | Channel dimensions and liquid properties

Channel geometry	Liquid properties
Half-angle $\alpha = 30°$	Density $\rho = 935.3134\ \mathrm{kg/m^3}$
Vane width $b = 35\mathrm{mm}$	Kinematic viscosity $\nu = 1\times10^{-5}\ \mathrm{m^2/s}$
Vane length $L = 110\mathrm{mm}$	Surface tension $\sigma = 0.0201\ \mathrm{N/m}$
Tank inner diameter $2R = 116\mathrm{mm}$	Contact angle $\theta = 0^{\circ}$

415

416 The three-dimensional simulations used the InterFoam solver of the open-source software
417 OpenFOAM, which tracks the gas–liquid interface with the VOF method and solves the
418 governing equations of incompressible two-phase flow; both phases were treated as

incompressible and the flow was assumed to be isothermal. To reduce the computational cost, the geometric model was simplified to a 1/12 model, as shown in Fig. 14b; symmetry conditions were applied on the symmetry planes and at the perforations, and no-slip conditions on the container walls and vane surfaces. A mesh-convergence study set the maximum cell size in the fluid domain to $\Delta x \leq 1$ mm, giving a final mesh of about 1.44 million cells. The initial liquid height in the container was 20 mm and the total simulated time was 3.5 s.

Drop-tower experiment

The microgravity environment was provided by the 3.5 s drop tower of the Institute of Mechanics, Chinese Academy of Sciences. A double-capsule drop assembly was used to reduce the influence of air drag on the experiment, and the microgravity level reached 10^{-5} g . The test articles were manufactured by 3D printing from a transparent resin, as shown in Fig. 15, and filled with Shin-Etsu KF-96-10cst silicone oil as the working liquid, whose contact angle with the wall of the article is 0°.

The article was fixed on a platform inside the drop capsule, with vanes of different perforation ratios installed inside and a fixed volume of silicone oil. Before release, the liquid collected at the bottom of the article under gravity; once the capsule was released and entered free fall, surface tension replaced gravity as the dominant force controlling the flow, and the liquid climbed along the interior-corner channel of the vane. The whole process was recorded by a camera mounted on the platform at 60 frames per second, and the surface position at each instant was extracted by image recognition to give the flow distance as a function of time.

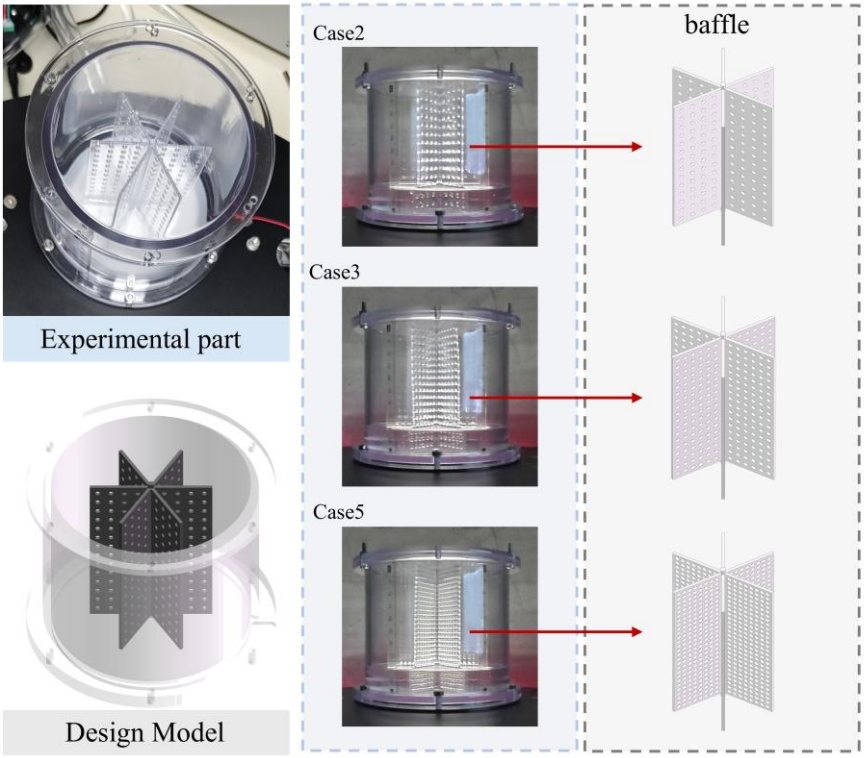


Fig. 15 | Schematic of the test article

Data availability

The experimental and simulation data supporting this study are available from the corresponding author on reasonable request.

Code availability

All relevant codes for the image analysis protocols are available from the corresponding authors upon request.

Acknowledgements

This research is supported by the National Natural Science Foundation of China (Grant No.52105290 and No. 62373276).

Author contributions

Z. Wu, and B. Wu wrote the main manuscript text. Y. Zhang and C. Fan participated in the drop-tower experiment. C. Jiang took part in the numerical simulation. Y. Chen, Y. Zhao and Y. Bai supervised the theoretical methods and the experiments. All authors reviewed the manuscript.

Competing interests

The authors declare no competing interests.

References

1. Jaekle, D., Jr. Propellant management device conceptual design and analysis - Vanes. in *27th Joint Propulsion Conference* (American Institute of Aeronautics and Astronautics, Sacramento, CA, U.S.A., 1991). doi:10.2514/6.1991-2172.
2. Weislogel, M. M. & Collicott, S. H. Capillary rewetting of vaned containers: spacecraft tank rewetting following thrust resettling. *AIAA Journal* **42**, 2551–2561 (2004).
3. Collicott, S. Initial experiments on reduced-weight propellant management vanes. in *35th Intersociety Energy Conversion Engineering Conference and Exhibit* (2000).
4. Liu, J. *et al.* Experimental Study on Liquid Sloshing of a Vane-type Surface Tension Tank for Satellite. *Microgravity Sci. Technol.* **34**, 83 (2022).
5. Li, G., Huang, Y., Han, W., Wu, Z. & Yang, Y. Space Liquid Transport Experiments in Tianyuan-1. *Microgravity Sci. Technol.* **34**, 100 (2022).
6. Chen, S. *et al.* Study on the shape and motion of bubbles in the tank model with a central column aboard the Chinese Space Station. *Physics of Fluids* (2024).
7. Chen, S. *et al.* Study on Liquid Climbing Behavior During Filling Process in Tank Models Aboard the Chinese Space Station. *Microgravity Sci. Technol.* **36**, 36 (2024).
8. Kolliopoulos, P. & Kumar, S. Capillary flow of liquids in open microchannels: overview and recent advances. *npj Microgravity* **7**, 51 (2021).
9. Weislogel, M. M. Capillary flow in containers of polygonal section. *AIAA Journal 39*, 2320–2326 (2001).
10. Weislogel, M. M. & Lichter, S. Capillary flow in an interior corner. *J. Fluid Mech.* **373**, 349–378 (1998).
11. Chen, Y., Weislogel, M. M. & Nardin, C. L. Capillary-driven flows along rounded interior corners. *Journal of Fluid Mechanics* **566**, 235–271 (2006).
12. Concus, P. & Finn, R. On the Behavior of a Capillary Surface in a Wedge. *Proceedings of the National Academy of Sciences of the United States of America* **63**, 292–299 (1969).
13. Ayyaswamy, P. S., Catton, I. & Edwards, D. K. Capillary Flow in Triangular Grooves. *Journal of Applied Mechanics* **41**, 332–336 (1974).
14. Lenormand, R. & Zarcone, C. Role of roughness and edges during imbibition in square capillaries. in *59th Annual Technical Conference and Exhibition* (1984).
15. Dong, M. & Chatzis, I. The Imbibition and Flow of a Wetting Liquid along the Corners of a Square Capillary Tube. *Journal of Colloid and Interface Science* **172**, 278–288 (1995).

16. Romero, L. A. & Yost, F. G. Flow in an open channel capillary. *Journal of Fluid Mechanics* **322**, 109–129 (1996).
17. Weislogel, M. M. & McCraney, J. T. The symmetric draining of capillary liquids from containers with interior corners. *J. Fluid Mech.* **859**, 902–920 (2019).
18. Kang, Q., Hou, R., Duan, L. & Hu, L. Capillary flow along rounded interior corner of right angle under microgravity. in *ICEM 2008: International Conference on Experimental Mechanics 2008* (2008).
19. Ramé, E. & Weislogel, M. M. Gravity effects on capillary flows in sharp corners. *Physics of Fluids 21*, 042106–042117 (2009).
20. Li, J., Chen, X., Huang, Y. & Bai, Y. Study on asymmetric interior corner flow in microgravity condition. *Science China Technological Sciences* 2332–2337 (2012).
21. Li, Y. *et al.* Study of Capillary Driven Flow in an Interior Corner of Rounded Wall Under Microgravity. *Microgravity Sci. Technol.* **27**, 193–205 (2015).
22. Wu, Z., Huang, Y., Chen, X. & Zhang, X. Capillary-driven flows along curved interior corners. *International Journal of Multiphase Flow* **109**, 14–25 (2018).
23. Wu, Z. *et al.* Corner angle effects on capillary rise along curved interior corners. *npj Microgravity* **11**, 67 (2025).
24. Chen, S. *et al.* Capillary phenomena in the corner of truncated-cone-shaped containers under microgravity. *Acta Mech. Sin.* **39**, 322347 (2023).
25. Chen, S. *et al.* Profiles of Liquid on the Surface of Revolution with Varying Cross-section under Microgravity. *Microgravity Sci. Technol.* **34**, 106 (2022).
26. Fiorini, D. *et al.* Characterization of a Capillary-Driven Flow in Microgravity by Means of Optical Technique. *Multiphase Science and Technology* **35**, (2023).
27. Chen, S., Duan, L., Li, W., Chen, S. & Kang, Q. Profiles of free Surfaces in Revolved Containers Under Microgravity. *Microgravity Sci. Technol.* **36**, 11 (2024).
28. Wu, B., Wu, Z., Chen, Y., Li, G. & Yao, W. Free surface bubbly flow in an open capillary channel. *npj Microgravity* **11**, 43 (2025).
29. Lin, S. *et al.* Experimental Investigation of Diamagnetic Fluids With Magnetically Compensated Effective Gravity. *Microgravity Sci. Technol.* **38**, 16 (2026).
30. de Lazzer, A., Langbein, D., Dreyer, M. & Rath, H. J. Mean curvature of liquid surfaces in cylindrical containers of arbitrary cross-section. *Microgravity Science and Technology* 208–219 (1996).